Title: **Crack growth resistance of MAG butt-welded joints of S355JR construction steel**

Authors: **M. Benedetti, V. Fontanari, C. Santus**

DOI Link: https://doi.org/10.1016/j.engfracmech.2013.01.019

Crack growth resistance of MAG butt-welded joints of S355JR construction steel

M. Benedetti[1*], V. Fontanari[1], C. Santus[2]

[1]Department of Industrial Engineering, University of Trento, via Mesiano 77, 38123 Trento, Italy

[2]Department of Mechanical, Nuclear and Production Engineering, University of Pisa, largo Lucio Lazzarino 1, 56126 Pisa, Italy

* Contacting Author:

Matteo Benedetti

Tel. +390461282457

Fax +390461281977

E-mail: matteo.benedetti@ing.unitn.it

Abstract

Fatigue crack growth resistance and elastic-plastic fracture toughness were measured on MAG (Metal Active Gas) butt-welded joints made of S355JR construction steel. For this purpose, C(T) specimens were extracted from virgin and welded 15 mm thick rolled plates. Tests were conducted on the base material (BM), the heat affected zone (HAZ) and weld metal (WM). The analyses showed that compressive residual stresses due to welding increased the fatigue crack growth resistance of WM and HAZ owing to crack closure effects. The WM displayed the lowest elastic-plastic fracture toughness with respect to HAZ and BM. The highest value was exhibited by the HAZ because stable tearing crack extension is forced along an unfavourable crack path. Therefore, particular care must be taken in evaluating the crack path in welded joints in order to correctly estimate their resistance to crack advance.

Keywords: Welded joints; MAG; S355JR construction steel; fatigue crack growth resistance; elastic-plastic fracture toughness

1. Introduction

Welded joints are commonly used in structural and mechanical engineering because of several advantages with respect to other joining and manufacturing techniques: (i) no flanges or parts overlap is needed in contrast to bolted joints, resulting in lighter construction and materials savings; (ii) components of complex shapes can be obtained by joining simpler mechanical details, thus reducing machining time and costs as well as material waste; (iii) welding can be done *in situ* where the component must be installed, thus facilitating the transportation of large civil infrastructures. On the other hand, welding can be quite cumbersome for some reasons: (i) welding creates a permanent joint, not desirable if parts need to be fixed or replaced later; (ii) welding very thin sheets is difficult, in some situation riveted or bolted joints are more cost-effective for thin sheet metal; (iii) welding requires much more hands-on oversight than other methods, and much stricter manufacturing controls, involving a great deal of training and expertise; (iv) welding can result in distortion due to residual stresses; (v) the mechanical resistance of welded joints is hardly predictable due to defects, residual stresses, metallurgical modifications and a complex stress state induced by the local geometry of the weld toe.

Nowadays, the major part of welded joints is fabricated through MIG/MAG techniques, where the consumable metal electrode is both filler material and arc carrier. The "endless" filler wire is fed into the welding torch, where the current is transferred at the so-called contact tube. The free wire end is concentrically surrounded by a gas nozzle. The shielding gas that flows out prevents chemical reactions between the hot workpiece surface and the surrounding atmosphere. This maintains the strength and durability of the weld metal. Inert and active gases can be used as shielding gases. The Metal Active Gas (MAG) process uses an active gas, generally a mixture of carbon dioxide and argon, instead of the pure inert gas used in the standard Metal Inert Gas (MIG) process. The MAG process, commonly used in structural steel work, is cheaper than the argon-shielded welding process and in certain applications provides deeper penetration and an increase in welding speed [1-3].

During the last decades, many efforts have been devoted to improve the structural integrity assessment of welded joints. On one side, the reliability and repeatability of welding joints have been improved through controlled and mechanized processes [1]. On the other side, more and more sophisticated fatigue verification criteria of welded joints have been developed and frequently incorporated in important design codes. In general, they can be subdivided into several categories according to the parameters assumed to be meaningful for the joint fatigue behaviour: nominal stress [4,5], structural or hot-spot stress [6,7], notch stress and notch intensity [8,11], notch strain or equivalent strain energy density [12,13], crack propagation [14,15].

The latter criterion, based on the integration of the relationship between the rate of fatigue crack growth and the stress intensity factor range for the particular welded joint geometry being considered, is one of the most established. This obviously requires detailed characterization of the fracture toughness and fatigue crack growth resistance of welded joints in order to assess the critical crack size [16,17] and the time to propagation to this critical value. According to this approach, the fatigue life of welded joints is exclusively thought of as the propagation of cracks occurring at the toe and root of the weld seam up to a critical size leading to structural collapse or functionality loss. On one side, this assumption seems to be reasonable, since metallurgical analysis performed in cruciform joints made of construction steel confirmed the presence of inner technological defects at the weld root and toe whose average depth was about 0.10 – 0.15 mm [18]. On the other side, it has been found that the crack growth monotonically increases with the crack length only where the crack length was greater than 0.3 mm in depth; below this threshold, it was possible to find "small crack" behaviours, which cannot be described by simple Linear Elastic Fracture Mechanics (LEFM) relations, and the multiple crack interaction on different planes influenced by loading parameters and statistical variations related to the irregularity of the toe profile [19]. The problem can be practically overcome by increasing to some extension the initial crack length in crack propagation calculations [18], and by estimating the crack initiation time on the basis of different concepts [20]. Therefore, the total fatigue life is the sum of crack initiation life and crack propagation life.

Apart from overall fatigue life estimation, the crack propagation approach plays a key role in remaining fatigue life assessment and damage tolerant design to establish rational inspection planning of large welded structures. To this regard, in a recent paper [21], the authors explored the possibility of employing suitable strain sensors for structural health monitoring (SHM) of wind towers installed in complex terrains. For this purpose, the perturbation of the strain field in the vicinity of a crack located in the base welded joint, which is critical for the structural integrity of an existing wind tower, was numerically assessed. Several strategies for crack detection were investigated; the most promising of them is based on a radial arrangement of strain sensors around the tower periphery in the vicinity of the base welded joint. It has been found that (i) the major limiting factor for fatigue crack detection is the number of strain sensors, depending on the budget allocated for the health monitoring of the structure, rather than the strain sensor sensitivity; (ii) the minimum detectable crack size should be chosen on the basis of other considerations, like the compatibility between the residual service-life after damage detection, which in turn depends on the extreme wind conditions expected for the wind turbine, the inspection/maintenance schedule of the structure, and the crack growth resistance of the welded joint.

In the present paper, we address this latter issue by investigating the crack growth resistance of MAG butt-welded joints of S355JR steel, which is commonly used in metal carpentry and in structural applications, thanks to its excellent weldability. For this purpose, fracture mechanics tests are carried out using welded C(T) samples to quantify the resistance to fatigue crack growth as well as the elastic-plastic fracture toughness of weld joints. The paper is organized as follows. Section 2 describes the fabrication procedure of the C(T) specimens and the experimental procedures followed for determining the fatigue crack growth rates and the elastic-plastic fracture toughness in terms of *J*-resistance curves. Section 3 illustrates the experimental results and discusses them on the basis of crack path observations and residual stress measurements. The conclusions close the paper.

2. Experimental material and procedures

2.1 Base metal, welding and specimens

The material used in this study is the ferritic steel S355JR, supplied in the form of 15 mm thick rolled plate. The chemical composition of this material is indicated in Table 1. The results of three standard monotonic tensile tests (initial strain rate 1×10^{-3} s^{-1}), performed in the longitudinal (L) orientation using plane hourglass specimens, are summarized in Table 2.

Weld joints are fabricated by butting together two pieces of the original plate, which are previously chamfered to form a double V-groove that helps compensating for warping forces. Before welding, the two pieces are kept in place with an appropriate fixture to minimize the joint misalignment. The welding direction is normal to the rolling direction of the base material. The full penetration double welded butt joints are executed applying the metal-arc active gas (MAG), semi-automatic welding process with the active shielding gas Ar+10%CO_2 and direct current reverse polarity for deeper penetration. As filler material is used 1mm diameter wire EN 440- G42 4M G3Si1, whose mechanical properties declared by the supplier are: yield stress 420 MPa, ultimate tensile stress 500 MPa, total elongation 22%. Therefore, the strength mismatch factor, defined as the ratio between the weld metal and the base metal yield strength, is equal to 1.11, thus indicating about 10% over-matching.

The fracture mechanics tests are carried out on compact C(T) specimens whose geometry, according to the standard ASTM E1820-09 [22], is illustrated in Fig. 1a. They are extracted from the plates, as schematically shown in Fig. 1b, in order to introduce the fatigue crack starter notch (1) inside the Base Material (BM), (2) in the Weld Metal (WM) centre, (3) in the Heat Affected Zone (HAZ) along the weld bead. After machining, the specimens are grinded and polished to facilitate the monitoring of the crack advance. The initial notch of all

C(T) specimens is Electro Discharge Machined (EDM) with an EDM wire of 0.2 mm diameter to facilitate the follow-up pre-cracking process.

Metallographic samples are prepared and the weld microstructure is examined by optical microscopy. A Nital etching reagent is used to reveal microstructures. Cross-weld hardness profile is obtained at room temperature using a Vickers microharndess tester. An indentation load of 500 g and a time-dwell of 10 s are used. The indentations are spaced 0.2 mm apart, covering BM, HAZ and WM.

Residual stress profiles are measured along the depth through Blind Hole Drilling (BHD) technique in different spots with respect to the weld bead centreline using the test apparatus described in [23]. The holes are produced by means of a high- speed air turbine. The eccentricity is reduced through a monocular optical microscope with cross hairs to help the operator in aligning the drilling axis with the rosette centre. After drilling, the effective hole diameter and the residual hole eccentricity are measured using the optical microscope and two micrometric gauges placed on the guides aligned with the rosette axes. The zero depth is found by way of an electric contact between the tool and the metallic specimen surface. After the zero depth set-up, an electric stepping motor drives a calibrated screw system producing the hole depth increments. The actual hole increments are also measured by a micrometer with a digital gauge indicator. The strain gauges signals are averaged over 10 acquisitions during a total time of 0.3 s. The strain measurement is performed 3.0 s after each drilling operation, in order to let the temperature transient extinguish. Residual stresses are computed from the relaxed strain field according to the algorithm presented in [24].

2.2 Fatigue crack growth rate testing

The fatigue crack growth rate testing is performed according to the standard ASTM E647-08 [25]. The experiments are conducted in the laboratory environment on a 100 kN servo-hydraulic testing machine. A sinusoidal pulsating (load ratio R = 0.1) load waveform is applied at a frequency of 30 Hz. A travelling photomicroscopy apparatus, described in detail in [26], is used for crack length monitoring during fatigue tests. The crack length is measured on both specimen sides. The stress intensity factor and the crack growth rate are computed on the basis of the averaged value of the two surface crack lengths. The crack growth rate is computed through incremental polynomial method, fitting a second-order polynomial to sets of 3 successive data points.

The crack opening displacement is measured periodically (approximately every 0.5 mm crack advance) using a clip-on gauge across the crack mouth to determine the crack closure according to ASTM E-647-08, as described in [27].

After the fatigue tests, the specimens are sectioned by EDM along the thickness half-plane and metallographic samples are extracted in order to investigate the influence of the microstructure on the crack path.

2.3 Fracture toughness (J-Integral) testing

The fracture toughness testing is performed according to the standard ASTM E1820-09. The specimens are fatigue pre-cracked in the laboratory environment using a resonant testing machine with load ratio R = 0.1 keeping the maximum stress intensity factor less than 24 MPa√m. The initial crack length to specimen width ratio (a/W) is about 0.45. Particular care is taken to ensure that the crack sizes measured on front and back surface do not differ by more than 5% of the specimen thickness, otherwise the specimen is discarded. Subsequently, to enforce the plane strain condition, 20% V-notch side grooves are introduced, resulting in a net thickness (B_N) of 12 mm.

The single specimen method is adopted to determine the J-resistance curve J_R using a 100 kN servo-hydraulic testing machine. The crack opening displacement is recorded by a CMOD clip gauge during constant displacement rate (0.5 mm/min – under displacement gauge control). The load versus load line displacement measurements are performed by using a high-resolution clip on gauge. All data of load versus load line displacement and also the unloading/reloading data have been acquired with a sampling rate of 50 Hz. The resolution of the used clip on gauge fulfils the ASTM E1820-09 requirement with respect to the transducer specifications.

The crack length is measured after each CMOD increment of 0.2 mm by the unloading compliance technique and verified by post-test optical crack size measurements. For this purpose, in order to minimize the effect of load relaxation on the compliance measurements, causing a time-dependent nonlinearity in the unloading slope, leading for instance to apparent negative crack growth rates [28], the specimen is held at a constant CMOD for 1 min dwell time up to force stabilization prior to initiating the unloading. After the final unloading sequence, the specimen is again fatigued for further crack extension with the aim not to severely deform the crack extended region of the specimen for the later microscopic crack length measurement. The extended final crack length and the initial crack length positions have been determined using the ASTM E1820-09 standard procedure.

After the J-integral tests, the specimens are sectioned by EDM along the thickness half-plane and metallographic samples are extracted in order to investigate the influence of the microstructure on the crack path.

3. Results and discussion

3.1 Material characterization

Figure 2a illustrates the microstructural gradient observed in proximity of the weld joints. The average grain size of the BM, whose microstructure is shown in detail in Fig. 2b, is about 20 μm. By moving inwards to the HAZ, a change of microstructure is visible in Fig. 2c: the grains become smaller with about 5 μm and more equiaxed due to recrystallization. When moving further into the HAZ, the size of the grains increases due to the heating treatment related to the welding process. Fig. 2d shows the microstructure in the middle of the WM (fusion zone); it can be noted that the original austenitic grain structure (average grain size of about 80 μm) has been transformed during final cooling into acicular ferrite, whose plates are typically about 10 μm long and 1 μm wide.

Figure 3 illustrates the microhardness dependence upon the distance from the weld centre. It can be noted that the fusion material (WM) displays a microhardness significantly higher than the parent metal (BM), ranging between 270-280 $HV_{0.5}$ in WM and 200-210 $HV_{0.5}$ in the BM. The microhardness markedly increases in the HAZ, i.e. a transition region of about 2 mm width comprised between BM and WM. Apparently, WM and HAZ are hardened due to cooling after welding.

Figure 4a, b, and c illustrate the residual stress profiles measured along specimen depth in the BM, WM and HAZ, respectively. Because of the absence of martensitic transformation, as attested by metallographic analyses and microhardness measurements, residual stresses can be imputed to the differential cooling between surface and core after the welding process. The WM shows the highest compressive residual stresses, ranging between -330 MPa along the weld bead (x-) longitudinal direction and -160 MPa along the (y-) transverse direction. This latter residual stress component remains the in the compression domain down to 0.9 mm below the surface. The compressive residual stress field is less intense in the HAZ, amounting about -110 MPa along both directions. Compressive transverse residual stresses have been measured down to 0.8 mm below the surface. In addition, significant shear stresses have been measured throughout the specimen thickness. The BM shows compressive residual stresses in a region very close to the surface, i.e. about 0.2 mm deep.

3.2 Fatigue crack growth rates

The fatigue crack growth curves are plotted in Fig. 5a as a function of the stress intensity factor range. It can be noted that both WM and HAZ exhibit slower crack growth rates as compared to BM, especially in the near-threshold regime. This can be reasonably imputed to surface compressive residual stresses, responsible for crack

closure and thus crack growth retardation, which have been introduced by the welding process both in WM and HAZ as attested by BHD measurements. In Figure 5b, the fatigue crack growth curves are plotted as a function of the stress intensity factor range K_{eff} corrected for crack closure effects. Notably, the curves referring to the three material conditions tend to come closer, if compared to those of Fig. 5a, denoting that base and filler material possess similar fatigue crack growth resistance. In addition, crack growth rates are slower in HAZ than in WM and BM, even accounting for crack closure. A possible explanation thereof can be given by the analysis of the fatigue crack paths illustrated in Fig. 6a-c, for BM, WM, and HAZ, respectively. While crack propagation in BM and WM occurs on a plane approximately orthogonal to the loading direction, crack advance in HAZ occurs along an inclined direction, which is unfavourably oriented with respect to the stress axis. Apparently, the cracks initiated in the HAZ spontaneously tend to propagate outside the HAZ towards the BM, presumably because the shear residual stresses (shown in Fig. 4c) induce Mode II loading responsible for crack deflection [29].

3.3 J-resistance curves

The J_R curves are shown in Fig. 7. Significant stable tearing crack extension is observed for all tested specimens. In particular, the WM specimen exhibits the lowest fracture toughness. To this regard, it should be mentioned that only the test on the WM condition ended with a plane-strain fracture toughness value J_{Ic}, while BM and HAZ samples yielded thickness-dependent fracture toughness, this means that components with larger thickness might display smaller fracture toughness values. On the other hand, it has to be kept in mind that welded plates with thickness larger than 15 mm are rarely of practical interest, thus confirming the reasonableness of the obtained results.

It can be noted that the HAZ condition shows the highest J_c value. This can be explained by analysing the crack paths illustrated in Fig. 8a-c, for BM, WM, and HAZ, respectively. As expected, the fatigue precrack in BM and WM samples is orthogonal to the stress axis, while fatigue crack growth in HAZ occurred along an inclined plane due to the preferential propagation outside the HAZ. However, during the final monotonic loading, the crack path is rather dictated by the side grooves that have been machined after fatigue precracking. In this way, stable tearing crack extension is forced along an unfavourable crack path, resulting in a higher *J*-resistance curve.

This observation is further confirmed by an additional fracture toughness test conducted on a C(T) specimen where the crack starter notch has been machined inside the HAZ. In order to force also the fatigue precrack

along the sample centreline, V-notch side grooves have been machined prior to fatigue precracking. In this case, the fatigue crack advance has been monitored trough unloading compliance technique instead of visual inspection. The resulting J_R curve is compared in Fig. 9 with that measured on the first HAZ specimen, where the fatigue precrack was able to deviate from the specimen centreline. It can be noted that forcing the fatigue precrack along the specimen symmetry plane results in an even higher *J*-resistance curve, thus confirming the crucial role played by the crack path in determining the resistance to fatigue and stable tearing crack growth.

3.4 Discussion

On the basis of the experimental results shown before, the following observations can be made: (i) particular care must be taken in evaluating the crack path in welded joints in order to correctly estimate their resistance to crack advance; (ii) in contrast to the general opinion [30], the HAZ is not the critical part of this kind of welded joints, presumably because of absence of martensitic transformation, microstructurally unfavourable crack path and residual shear stresses responsible for fatigue crack deflection; (iii) the fracture mechanics tests are conducted in the present work on C(T) where the weld overfill has been removed by grinding; therefore the stress concentration effect exerted by the local geometry of the weld has not been taken into account; (iv) in welded mechanical components, fatigue cracks are likely to initiate in the HAZ because of the stress concentration at the weld toe, but then they spontaneously tend to propagate outside the HAZ; (v) therefore, the residual life estimation of the cracked welded component must take into account that the crack can propagate either in the WM at slower growth rates up to a critical size, which is smaller due to lower fracture toughness, or in the BM at higher growth rates but up to a larger critical size; (vi) welding residual stresses are responsible for fatigue crack growth retardation in WM and HAZ, resulting in a stress intensity factor threshold for fatigue crack propagation which is about two times larger than that corrected for crack closure effects. Therefore, the convenience of post-welding stress-relieving treatments is questionable in this kind of steels, since they are not affected by embrittlement due to martensitic transformation. On the other hand, the influence of residual stresses on the fatigue strength of real welded components must be carefully examined on a case-by-case. In fact, welding residual stresses (i) strongly depend on the structure geometry (mainly the thickness of the welded parts) that can be significantly different from that of the C(T) specimens used in the present work, and (ii) are affected by relaxation phenomena during in-service life [31,32].

4. Conclusions

Fatigue crack growth resistance and elastic-plastic fracture toughness were measured on MAG (Metal Active Gas) butt-welded joints made of S355JR construction steel. For this purpose, C(T) specimens were extracted from virgin and welded 15 mm thick rolled plates. Tests were conducted on the base material (BM), the heat affected zone (HAZ) and weld metal (WM). The following conclusions can be drawn:

a) Welding results in metallurgical modifications with respect to the base material: the WM displays acicular ferrite microstructure and the HAZ a very fine-grained ferritic structure. Both microstructures are harder than that of the BM due to the heat treatment related to welding.

b) Welding introduces surface compressive residual stresses, especially in WM and HAZ. In addition, significant residual shear stresses are present in HAZ throughout the thickness.

c) Compressive residual stresses are responsible for crack closure effects resulting in fatigue crack growth retardation in HAZ and WM with respect to the BM. Fatigue cracks tend to propagate outside the HAZ, presumably due to material-unfavourable crack path and residual shear stresses responsible for crack deflection.

d) The WM displays the lowest elastic-plastic fracture toughness with respect to HAZ and BM. The highest value is shown by the HAZ because stable tearing crack extension is forced along an unfavourable crack path.

References

[1] American Welding Society (AWS), *Welding Handbook*, Volume 2, Welding Processes Part 1, 9th Edition, ISBN 0-87171-729-8.

[2] Chiarelli M, Lanciotti A, Sacchi M. Fatigue resistance of MAG welded steel elements. Int J Fatigue 1999;21:1099-1110.

[3] Suban M, Tusek J. Dependence of melting rate in MIG/MAG welding on the type of shielding gas used. J Mat Proc Techn 2001;119:185-192.

[4] Gurney TR, Maddox SJ. A re-analysis of fatigue data for welded joints in steel. Welding Research Int 1973;3(4):1–54.

[5] Petinov SV, Reemsnyder HS, Thayamballi AK. The similitude of fatigue damage principle: application in S–N curves-based fatigue design. In: Marquis G, Solin S, editors. Fatigue design and reliability. Amsterdam: Elsevier, 1999.

[6] Radaj D, Sonsino CM. Fatigue assessment of welded joints by local approaches. Cambridge: Abington Publishers, 1998.

[7] Fricke W, Petershagen H. Detail design of welded ship structures based on hot spot stresses. In: Caldwell JB, Ward G, editors. Practical design of ships and mobile units. Amsterdam: Elsevier Science, 1992.

[8] Lazzarin P, Tovo R. A notch intensity factor approach to the stress analysis of welds. Fatigue Fract Engng Mat Struct 1998;21:1089–1103.

[9] Taylor D, Barrett N, Lucano G. Some new methods for predicting fatigue in welded joints. Int J Fatigue 2002;24:509-518.

[10] Susmel L. A novel engineering procedure to predict the lifetime of steel welded joints subjected to both uniaxial and multiaxial fatigue loading. Int J Fatigue 2008;30:888-907.

[11] Sonsino CM, Fricke W, de Bruyne F, Hoppe A, Ahmadi A, Zhang G. Notch stress concepts for the fatigue assessment of welded joints – Background and applications. Int J Fatigue 2012;34:2-16.

[12] Sonsino CM. Multiaxial fatigue of welded joints under in-phase and out-of-phase local strains and stresses. Int J Fatigue 1995;17(1):55–70.

[13] Livieri P, Lazzarin, P. Fatigue strength of steel and aluminium welded joints based on generalised stress intensity factors and local strain energy values. Int J Fracture 2005;133:247-276.

[14] Maddox SJ. Calculating the fatigue strength of a welded joint using fracture mechanics. Metal Construction 1970;2(8):327–31.

[15] Fischer C, Feltz O, Fricke W, Lazzarin P. Application of the Notch Stress Intensity and Crack Propagation Approaches to Weld Toe and Root Fatigue. Welding in the world 2011;55:30-39.

[16] R6. Assessment of the Integrity of Structures Containing Defects, Nuclear Electric Procedure R/H/R6, Revision 4, 2001.

[17] Kumar V, German MD, Shih CF. An Engineering Approach for Elastic-Plastic Fracture Analysis, EPRI, Final Report to NP 1931, 1981.

[18] Maddox SJ. The Effect of Plate Thickness on the Fatigue Strength of Fillet Welded Joints, Abington Publishing, Abington, Cambridge, 1987.

[19] Atzori B, Lazzarin P, Tovo R. From a local stress approach to fracture mechanics: a comprehensive evaluation of the fatigue strength of welded joints. Fatigue Fract Engng Mat Struct 1999;22:369–381.

[20] Hou CY, Charng JJ. Models for the estimation of weldment fatigue crack initiation life. Int. J. Fatigue 1997;19:537–541.

[21] Benedetti M, Fontanari V, Zonta D. Structural health monitoring of wind towers: remote damage detection using strain sensors. Smart Mater Struct 2011;20:055009.

[22] ASTM E1820 – 09. Standard Test Method for Measurement of Fracture Toughness. ASTM International, West Conshohocken, PA, USA, 2009.

[23] Valentini E, Benedetti M, Fontanari V, Beghini M, Bertini L, Santus C. Fine increment hole- drilling method for residual stress measurement, proposal of a calibrating apparatus. Book Experimental Analysis of Nano and Engineering Materials and Structures. Springer, Netherlands, 2007.

[24] Valentini E, Beghini M, Bertini L, Santus C, Benedetti M. Procedure to Perform a Validated Incremental Hole Drilling Measurement: Application to Shot Peening Residual Stresses. Strain 2010;47:e605-e618.

[25] ASTM E647 – 08. Standard Test Method for Measurement of Fatigue Crack Growth Rates. ASTM International, West Conshohocken, PA, USA, 2008.

[26] Benedetti M, Bertini L, Fontanari V. Behaviour of fatigue cracks emanating from circular notches in Ti–6Al–4V under bending. Fatigue Fract Engng Mat Struct 2004;27:111–125.

[27] Benedetti M, Heidemann J, Peters JO, Lütjering G. Influence of sharp microstructural gradients on the fatigue crack growth resistance of $\alpha+\beta$ and near-α titanium alloys. Fatigue Fract Engng Mat Struct 2005;28:909–22.

[28] Weiss K, Nylas A. Specific aspects on crack advance during J-test method for structural materials at cryogenic temperatures. Fatigue Fract Engng Mat Struct 2006;29:83-92.

[29] Benedetti M, Beghini M, Fontanari V, Monelli B. Fatigue cracks emanating from sharp notches in high-strength aluminium alloys: The effect of loading direction, kinking, notch geometry and microstructure. Int J Fatigue 2009;31:1996–2005.

[30] Zhang ZL, Thaulow C, Hauge M. Effects of crack size and weld metal mismatch on the HAZ cleavage toughness of wide plates. Eng Fract Mech 1997;57:653-664.

[31] McLung RC. A literature survey on the stability and significance of residual stresses during fatigue. Fatigue Fract Eng Mater Struct 2007;30:173–205.

[32] Benedetti M, Fontanari V, Scardi P, Ricardo CLA, Bandini M. Reverse bending fatigue of shot peened 7075-T651 aluminium alloy: The role of residual stress relaxation. Int. J. Fatigue 2009;31:1225-1236.

Tables

Table 1. Chemical composition of the S355JR steel (w/%).

C	Mn	Si	S	P	Al	Cu	Ni
0.16	1.12	0.245	<0.001	0.014	0.026	0.151	0.325

Table 2. Monotonic tensile properties of the S355JR steel.

E (GPa)	σ_Y (MPa)	σ_{UTS} (MPa)	T.E. (%)
205±2	380±5	560±5	30±5
E: elastic modulus; σ_Y 0.2% yield strength; σ_{UTS} ultimate tensile strength; T.E. total elongation			

Figure captions

Figure 1. Geometry of C(T) specimens used in this study. (b) Extraction scheme from the welded plates.

Figure 2. Optical micrograph of the microstructure of the welded joint (etching with 2% Nital reagent). WM: Weld Metal, HAZ: Heat Affected Zone, BM: Base Material. (a) Overall view, (b) detail of base material, (c) heat affected zone, and (d) weld metal.

Figure 3. Hardness profile measured along a direction normal to the weld bead.

Figure 4. Residual stress profiles measured using the BHD technique in different spots of the welded joints. (a) Base Material, (b) Weld Metal, (c) Heat Affected Zone. The *x*-axis is oriented along the longitudinal, the *y*-axis with the transverse direction of the weld bead. The location of the measurement spot with respect to the welded joint is indicated in the corresponding figure.

Figure 5. Fatigue crack growth curves plotted as a function of the (a) nominal and (b) effective stress intensity factor range.

Figure 6. Fatigue crack paths obtained after fatigue tests by sectioning the C(T) specimens by EDM along the thickness half-plane. (a) Base Material, (b) Weld Metal, (c) Heat Affected Zone. The metallographic samples are etched using 2% Nital reagent.

Figure 7. *J*-resistance curves obtained after *J*-resistance tests by monotonic loading C(T) that have been previously fatigue precracked. V-notch side grooves are machined after fatigue precracking.

Figure 8. Fracture crack paths obtained by sectioning the C(T) specimens by EDM along the thickness half-plane. (a) Base Material, (b) Weld Metal, (c) Heat Affected Zone. The metallographic samples are etched using 2% Nital reagent.

Figure 9. Effect of crack path on the J-resistance curves of the HAZ. V-notch side grooves have been machined either after or before fatigue precracking. In the first case the fatigue crack spontaneously tends to grow outside the HAZ towards the BM, whereas in the second case it is forced to propagate along the specimen centreline.

Figures

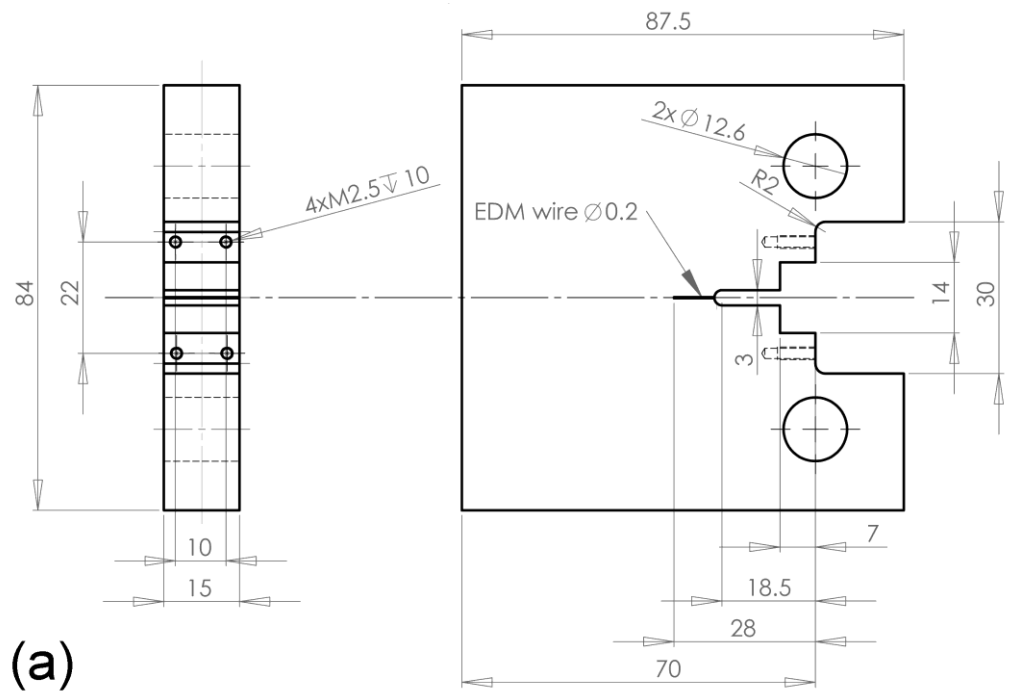

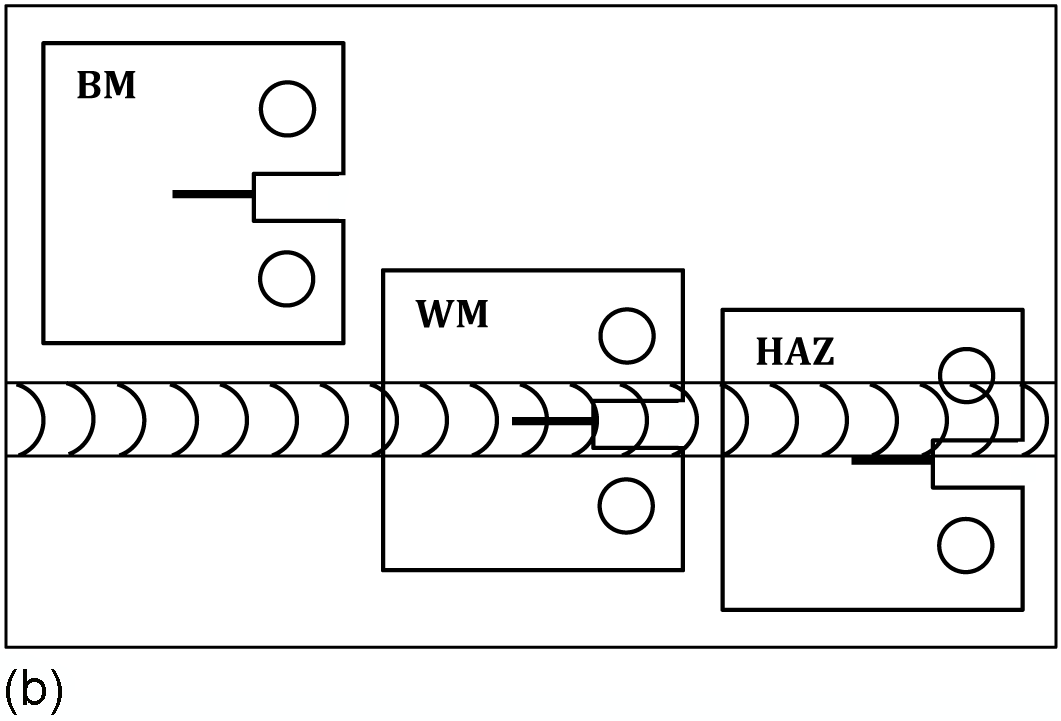

Figure 1.

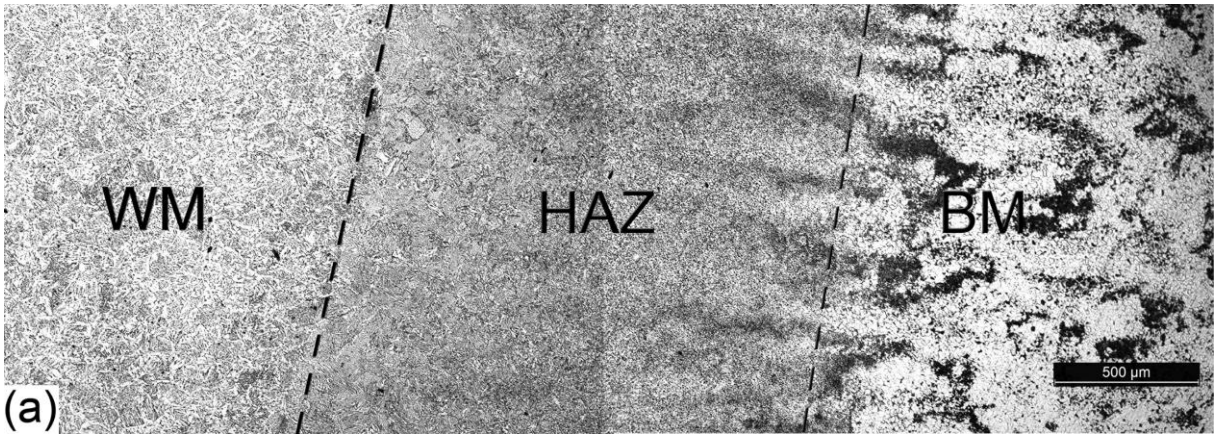

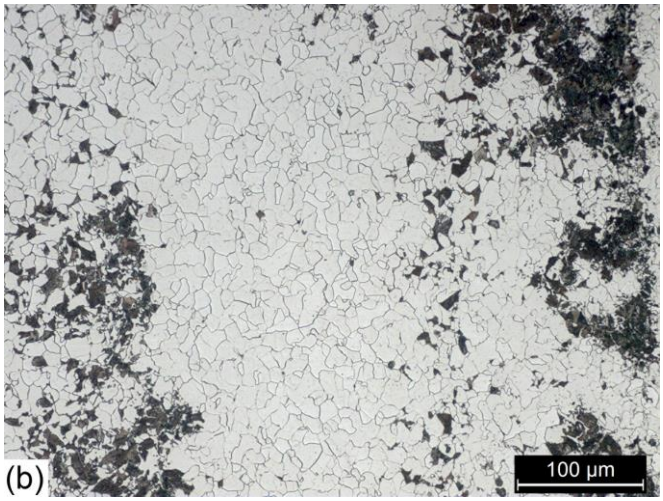

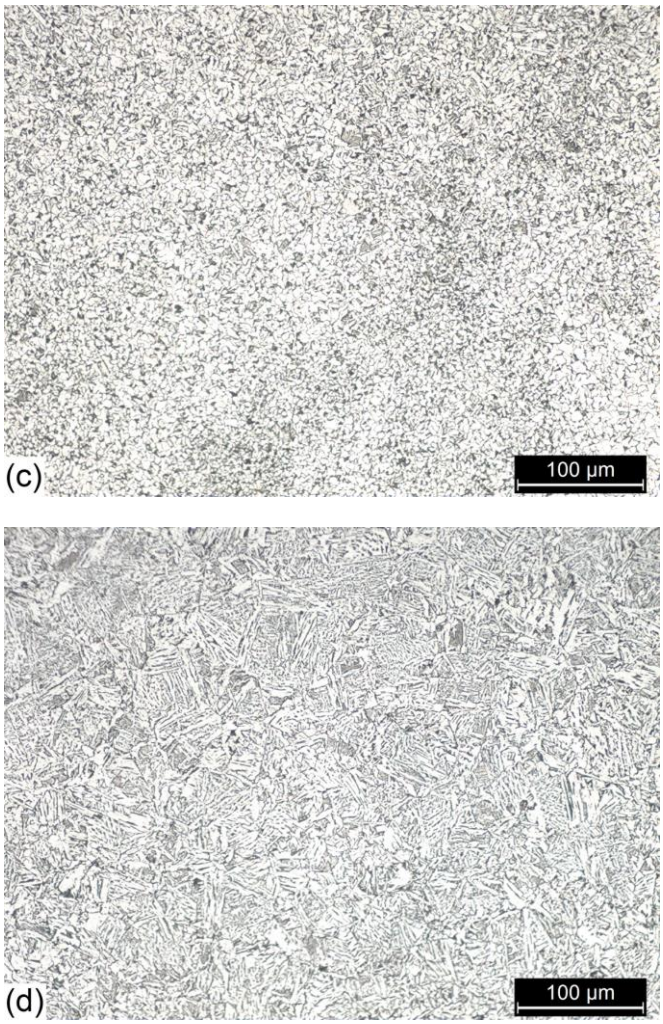

Figure 2.

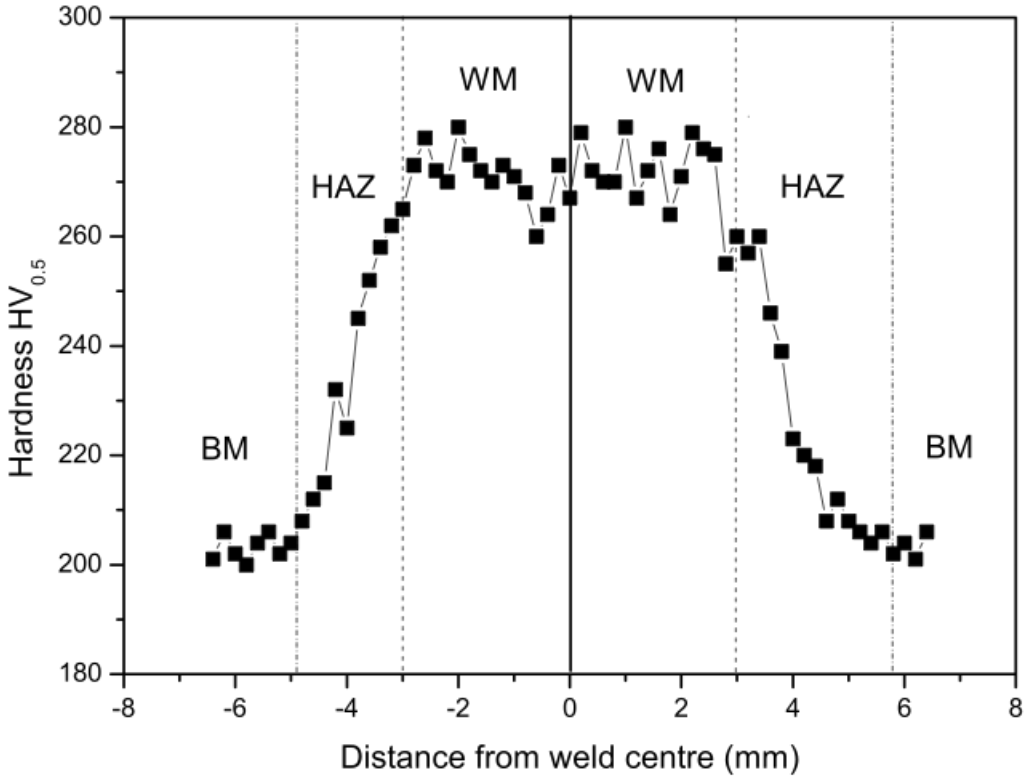
WM
WM
HAZ
HAZ
BM
BM
Hardness HV0.5
Distance from weld centre (mm)

Figure 3.

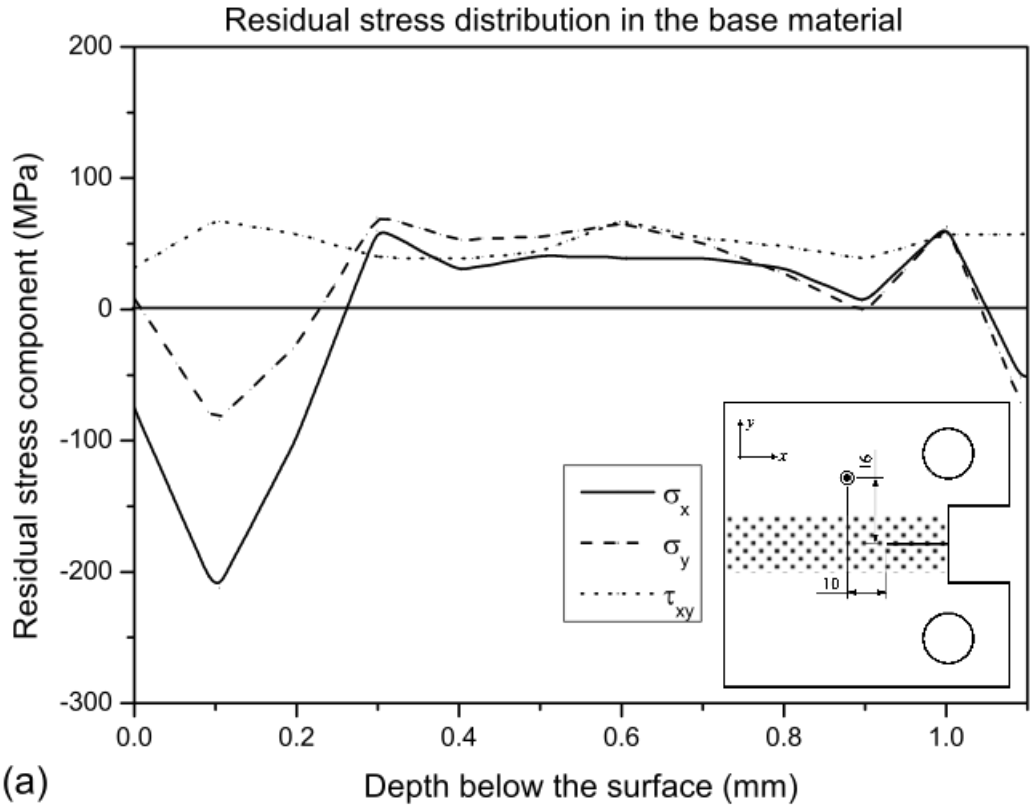
Residual stress distribution in the base material
Residual stress component (MPa)
Depth below the surface (mm)
σx
σy
τxy
16
10
(a)

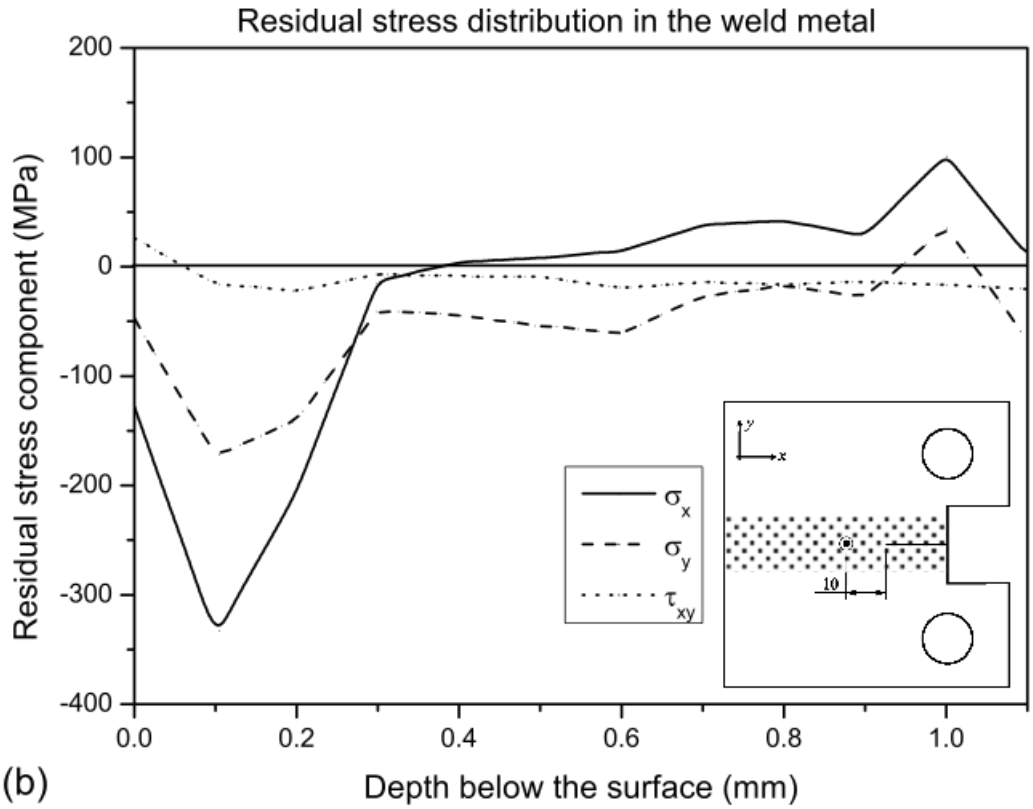
Residual stress distribution in the weld metal
Residual stress component (MPa)
Depth below the surface (mm)
σx
σy
τxy
10
(b)

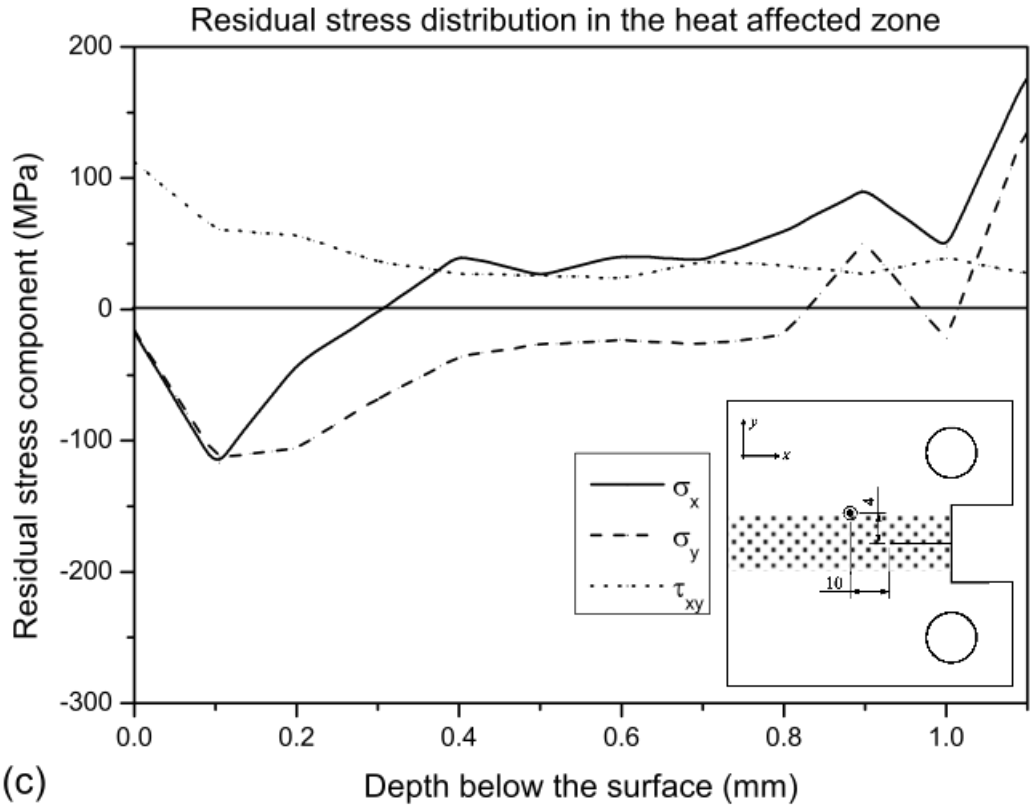
Residual stress distribution in the heat affected zone
Residual stress component (MPa)
Depth below the surface (mm)
σx
σy
τxy
10
(c)

Figure 4.

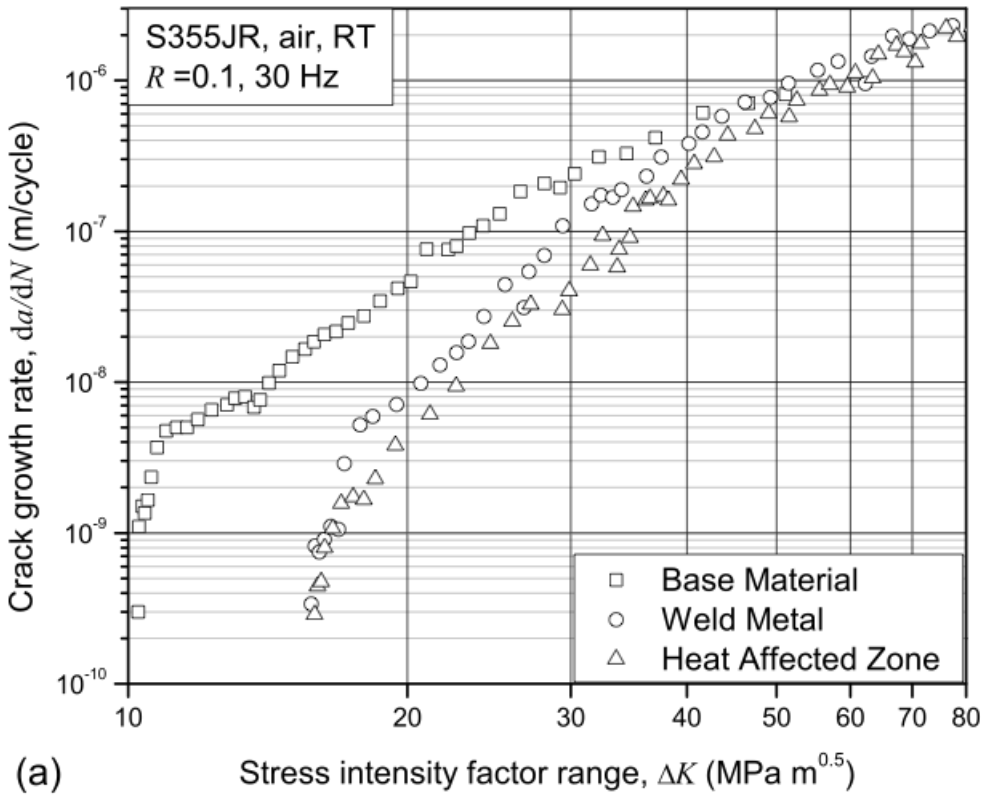
S355JR, air, RT
R =0.1, 30 Hz
Crack growth rate, da/dN (m/cycle)
Base Material
Weld Metal
Heat Affected Zone
(a)
Stress intensity factor range, ΔK (MPa m^0.5)

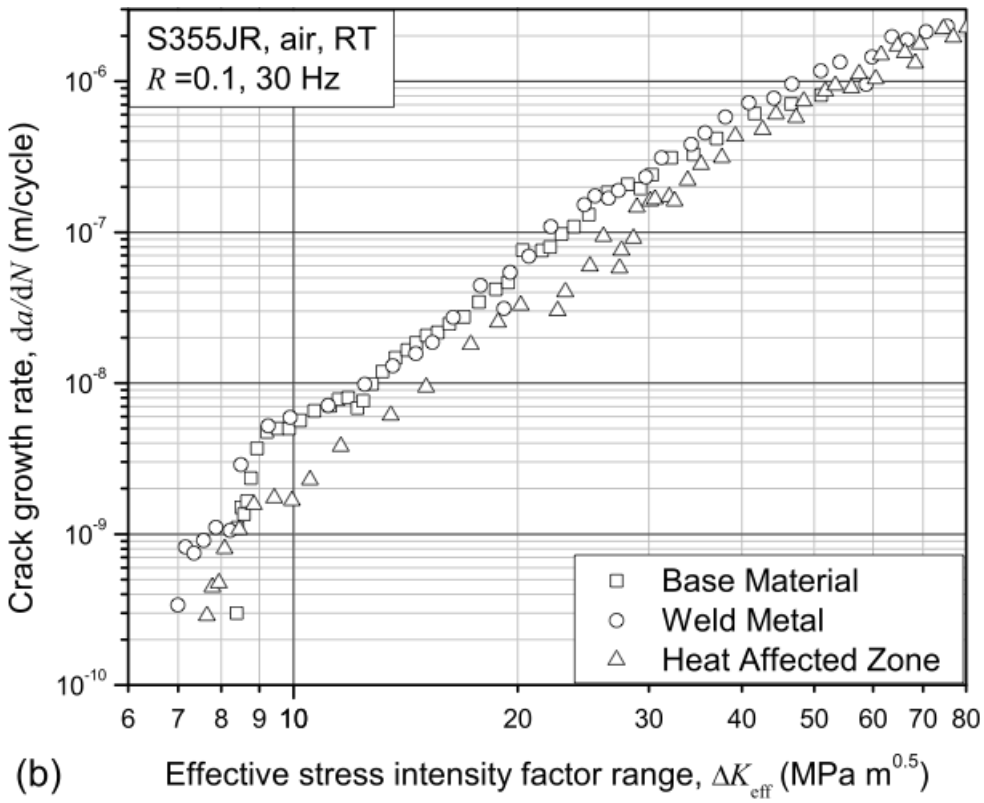
S355JR, air, RT
R =0.1, 30 Hz
Crack growth rate, da/dN (m/cycle)
Base Material
Weld Metal
Heat Affected Zone
(b)
Effective stress intensity factor range, ΔK_eff (MPa m^0.5)

Figure 5.

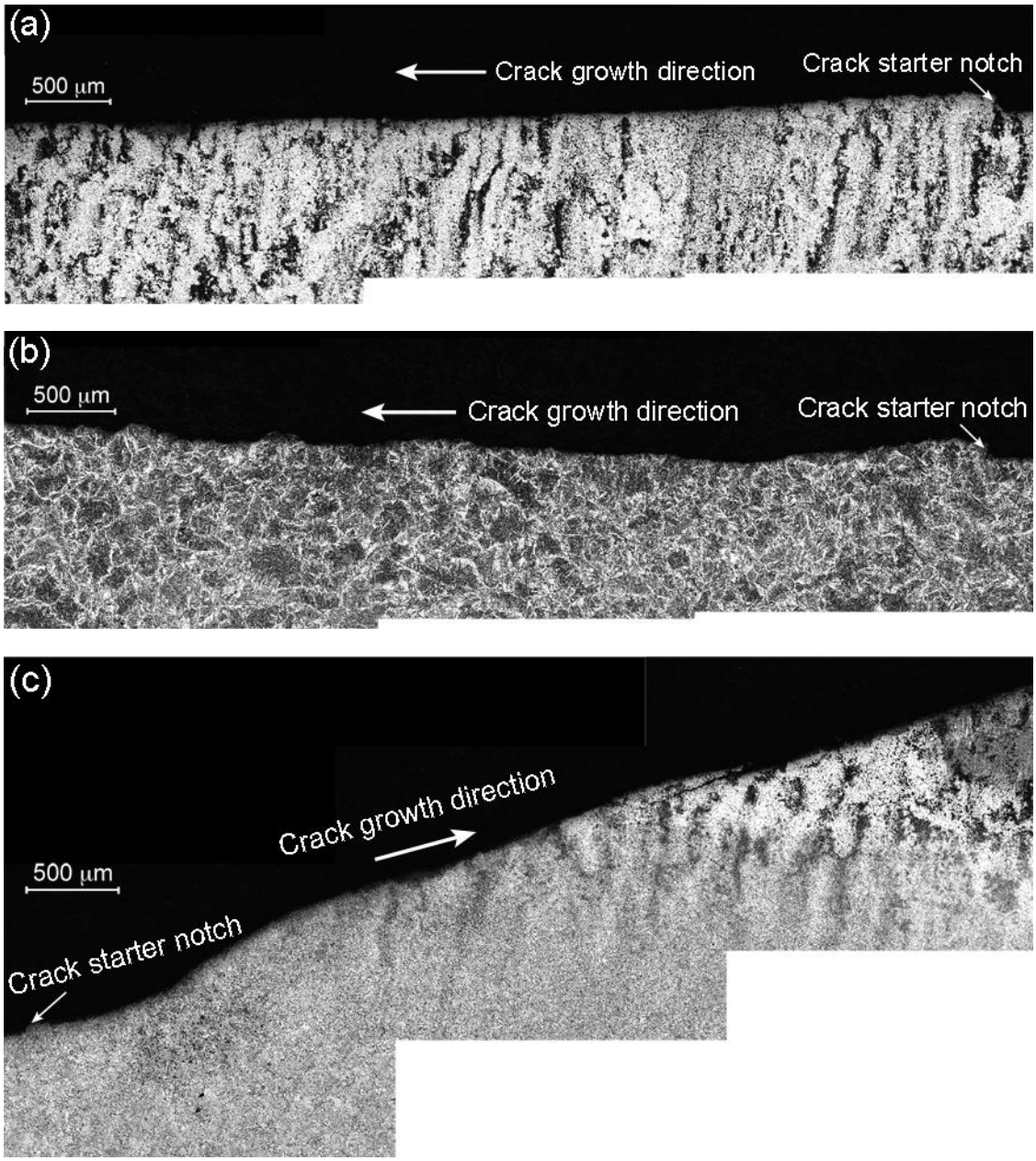
(a)
500 μm
Crack growth direction
Crack starter notch
(b)
500 μm
Crack growth direction
Crack starter notch
(c)
Crack growth direction
500 μm
Crack starter notch

Figure 6.

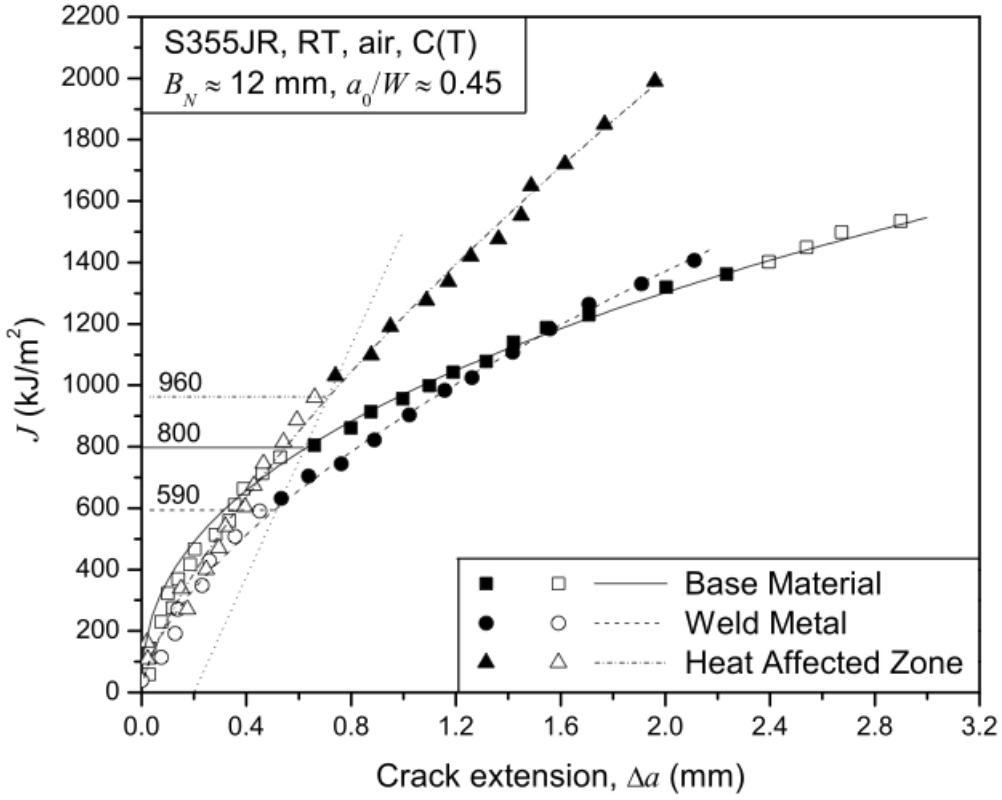
S355JR, RT, air, C(T)
$B_N \approx 12$ mm, $a_0/W \approx 0.45$
960
800
590
Base Material
Weld Metal
Heat Affected Zone
J (kJ/m^2)
Crack extension, Δa (mm)
0
200
400
600
800
1000
1200
1400
1600
1800
2000
2200
0.0
0.4
0.8
1.2
1.6
2.0
2.4
2.8
3.2

Figure 7.

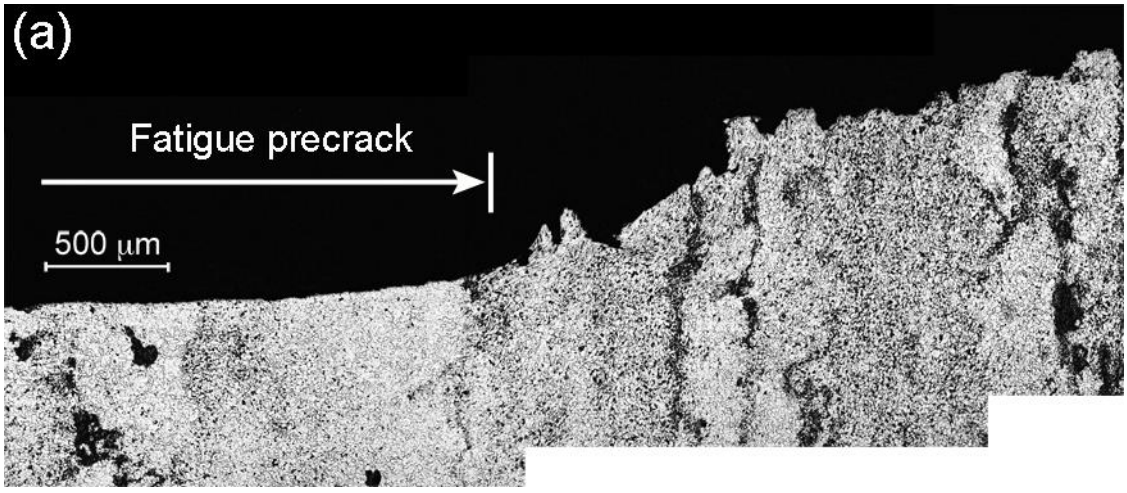
(a)
Fatigue precrack
500 μm

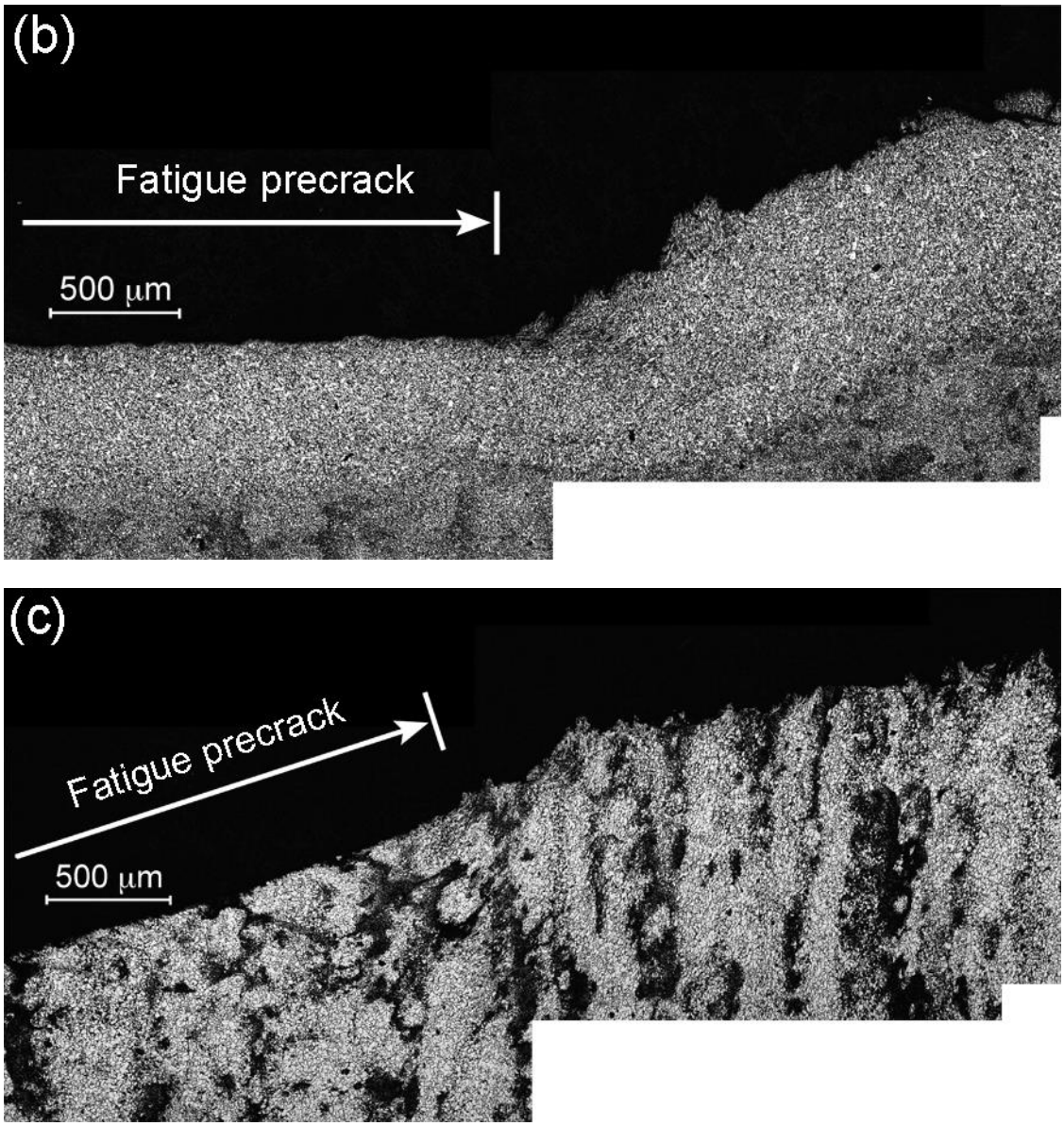

Figure 8.

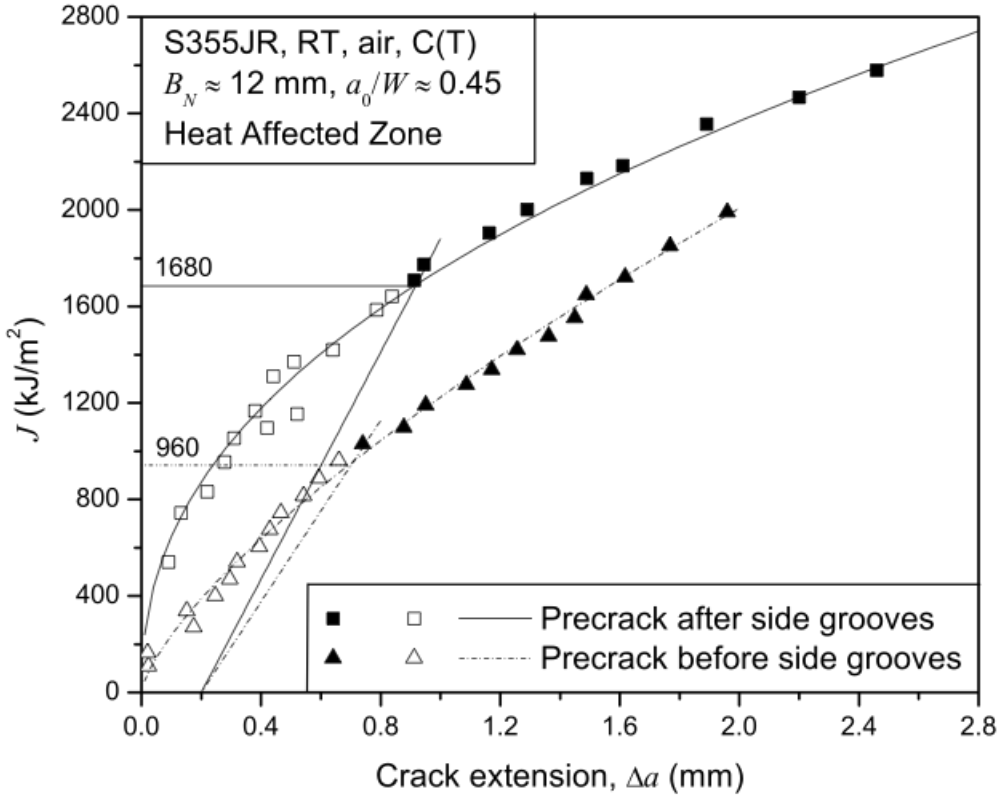
S355JR, RT, air, C(T)
$B_N \approx 12$ mm, $a_0/W \approx 0.45$
Heat Affected Zone
1680
960
Precrack after side grooves
Precrack before side grooves
J (kJ/m^2)
Crack extension, Δa (mm)
0
400
800
1200
1600
2000
2400
2800
0.0
0.4
0.8
1.2
1.6
2.0
2.4
2.8

Figure 9.